Energetic neutral atoms at Mars 1. Imaging of solar wind protons

Mats Holmström and Stas Barabash Swedish Institute of Space Physics, Kiruna, Sweden

Esa Kallio

Finnish Meteorological Institute, Geophysical Research, Helsinki, Finland

Received 28 September 2001; revised 17 January 2002; accepted 17 January 2002; published XX Month 2002.

[1] Energetic neutral atom (ENA) images are computed from an empirical solar wind proton model and recent models of the Martian exosphere. The proton model describes the proton bulk velocity in the interaction region and the neutral model the profiles of H, H₂ and O (hot) and O (thermal). We assume a Maxwellian proton velocity distribution. The ENA production model is analytical; thus an ENA image can be constructed for any vantage point by line of sight integration, and we present examples of such images. In this work we study the influence of different parameters in the input models on the generated images and examine the relative importance of the different parameters on the global ENA production rate as well as on image morphology for particular vantage points. All together our parameter set includes 14 variables for solar wind conditions, flow geometry, and the exosphere model. Changing the parameters also makes it possible to mimic various features of the solar wind-Mars interaction, such as some of the effects caused by the recently observed magnetic anomalies. It is found that the exobase temperature of atomic hydrogen is the parameter that affects the ENA production and images most. We also investigate the backscattering of ENAs that precipitate on the Martian atmosphere. It is found to be an important effect for views of Mars in the antisunward direction. The outflux of ENAs from the near Mars region is studied, and two maxima are found. One at an angle of approximately 115° to the Mars-Sun line corresponding to ENAs produced downstream of the bow shock and one at approximately 150° corresponding to ENAs produced upstream of the bow shock in the solar wind. INDEX TERMS: 2780 Magnetospheric Physics: Solar wind interactions with unmagnetized bodies; 7837 Space Plasma Physics: Neutral particles; 6225 Planetology: Solar System Objects: Mars; 7843 Space Plasma Physics: Numerical simulation studies; KEYWORDS: solar wind-Mars interaction, energetic neutral atoms (ENA), charge exchange, ENA imaging

1. Introduction

[2] Where energetic ions meet neutral atoms, energetic neutral atoms (ENA) are created by charge exchange. Near the nonmagnetized planets the ENA production is large since the solar wind comes into direct contact with the lower parts of the planets' exospheres. This is in contrast to the situation at Earth where the magnetosphere shields most of the exosphere from the solar wind and only magnetospheric plasma can interact with the neutral gas [Roelof, 1987]. Barabash et al. [1995] first estimated the ENA fluxes near Mars. Further studies were made by Kallio et al. [1997] In this work we present a detailed study of the formation of hydrogen ENAs from solar wind protons. This is accomplished by investigating the effects of varying 14 parameters in an analytic interaction model. The ENA production model is based on that introduced by Kallio et al. [1997]. The energies of the produced ENAs are comparable to those of the original solar wind protons, typically around 1 keV and below.

- [3] We also study the flux of backscattered ENAs (or the ENA albedo) in our model. The existence of backscattered ENAs was predicted by *Kallio and Barabash* [2001]. In this work we present images of the ENA albedo.
- [4] There are three other accompanying papers on ENAs at Mars. *Mura et al.* [2002] study ENAs originating from the solar wind at Phobos. *Barabash et al.* [2002] consider oxygen ENAs from planetary oxygen ions, produced by photoionization. *Lichtenegger et al.* [2002] study hydrogen ENAs from pickup ions, where exospheric hydrogen is ionized, accelerated, and then charge exchanged.
- [5] To model the production of ENAs, one needs knowledge of the ion flux, the neutral densities and the charge-exchange cross sections. A production model can then be used to predict the ENA fluxes, and images of the ENA emissions can be computed. Such simulated images can help in interpreting large scale features in observed images. There are several approaches to generate images from production models. *Kallio et al.* [1997] uses a Monte Carlo

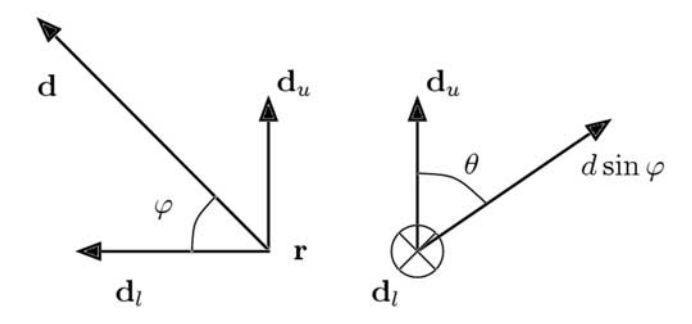


Figure 1. The view geometry for ENA images. For a given position \mathbf{r} , look direction \mathbf{d}_l , and up direction \mathbf{d}_u , an image is a two-dimensional function of the direction, \mathbf{d} , given by (φ, θ) , where φ is the angle of \mathbf{d} to \mathbf{d}_l , and θ is the angle between \mathbf{d}_u and the projection of \mathbf{d} onto a plane that is perpendicular to \mathbf{d}_l . The length of the projected vector is $d \sin \varphi$. Note that \mathbf{d} is not in the plane of \mathbf{d}_l and \mathbf{d}_u . We then perform a line of sight integration along the direction \mathbf{d} to compute the ENA flux from that direction $(1/(\text{cm}^2 \text{ sterad s}))$.

model, where individual ENAs are launched with probabilities proportional to the production rate, and then collected at the point where flux information is wanted. The advantage is that this is simple to implement. The drawback is that the error in the registered flux decreases slowly with the number of launched particles. In this work we use a different, continuous, approach, based on line of sight integration, where the ENA flux at a point is expressed as an integral along a view direction in the simulation domain. *Roelof* [1987] published an early example of such simulated ENA images, and the same method is used by *Mura et al.* [2002].

- [6] One advantage is that the method is faster if high accuracy is wanted. For a more detailed, quantitative, analysis of observed images one can use inversion techniques to extract parameters from a mathematical model. This involves the minimization of a function of ENA images. Since images generated by line of sight integration depend continuously on the parameters, it is the preferred approach for image inversion. Actually, the simulated images are analytical functions (albeit complicated) functions of the parameters. The first step in developing inversion techniques for ENA imaging of nonmagnetized planets is the generation of simulated, parameter dependent, ENA images. The images presented here will be compared to images observed by the two ENA imagers, parts of the Aspera-3 instrument (energy range 0.1-60 keV), on board ESA's Mars Express mission to be launched in 2003 [Barabash et al., 1998]. The model used here will be the base of software for parameter extraction from observed images.
- [7] First we describe the algorithm used for computing the ENA fluxes. Then we describe the image generation, investigate their parameter dependence, the ENA fluxes near Mars and the effect of ENAs backscattered by Mars' atmosphere.

2. Generating ENA Images

[8] In what follows, we denote vectors by boldface letters, e.g., **r** is the position vector. When a variable is used both

with and without boldface, standard typeface denotes the vector's magnitude, e.g., the distance to the center of Mars is $r = |\mathbf{r}|$. The coordinate system used is Cartesian and has the unit of Mars radii, $R_m = 3400$ km, with the origin at the center of Mars, the *x* axis in the sun direction and the *z* axis perpendicular to the plane of Mars' orbit.

[9] An ENA image, $w(\mathbf{r}, \mathbf{d})$, is a two-dimensional map of the ENA flux seen by an observer at position r looking in direction d (unit length). From now on, we simplify the notation by dropping the positional dependence, $w(\mathbf{d}) \equiv$ $w(\mathbf{r}, \mathbf{d})$. For a certain view, we can define a look direction, \mathbf{d}_{l} , and a perpendicular up direction, \mathbf{d}_{u} . Then the direction, **d**, can be specified by two angles. The angle, φ , between **d** and \mathbf{d}_l , and the angle, θ , between \mathbf{d}_u and the projection of \mathbf{d} onto a plane perpendicular to \mathbf{d}_{l} . All the images are presented in a polar format with the θ -coordinate as the polar angle and the φ -coordinate in the radial direction. The view geometry is illustrated in Figure 1. If we count all incoming ENAs, an image shows the number flux, $w(\theta, \phi)$ [1/(cm² sterad s)]. If we only consider incoming ENAs with energy E we have the differential flux, $w(\theta, \varphi, E)$ [1/(eV cm² sterad s)], i.e. the number of incoming ENAs in a small energy interval, ΔE , around E, is $w(\theta, \varphi, E) \Delta E$ and $w(\theta, \varphi) =$ $\int w(\theta, \varphi, E) dE$. The total influx of ENAs corresponding to an image is $\int w(\theta, \varphi) \sin \varphi \, d\varphi \, d\theta$.

[10] Since we assume the environment to be "optically" thin to ENAs, the differential flux, at position \mathbf{r} from direction (θ, φ) , is the line integral

$$w(\theta, \varphi, E) = \int_0^\infty g(\mathbf{r} + s\mathbf{d}, -\mathbf{d}, E)dS,$$

where $\mathbf{r} + s\mathbf{d}$ is the source location, $-\mathbf{d}$ is the emission direction, and E is the emission energy. The function $g(\mathbf{R}, \mathbf{D}, E)$ is the differential flux $[1/(eV \text{ cm}^3 \text{ sterad s})]$ of ENAs with energy E emitted from the position \mathbf{R} in the direction of \mathbf{D} .

[11] To generate a simulated ENA image we compute g from the ENA production rate $p(\mathbf{r})$ [1/(cm³ s)] and the proton bulk velocity $\mathbf{u}(\mathbf{r})$. We assume conservation of momentum and that the protons have a Maxwellian velocity distribution. Thus the ENAs will also have a Maxwellian velocity distribution,

$$f_{\text{ENA}}(\mathbf{v}, \mathbf{r}) = p \left(\frac{m}{2\pi kT}\right)^{3/2} e^{-\frac{m}{2kT}|\mathbf{v} - \mathbf{u}|^2},$$

where m is the proton mass, k is Boltzmann's constant, T the proton temperature and the ENA velocity $\mathbf{v}(\mathbf{d}, E) = \sqrt{2E/m}\mathbf{d}$. The temperature, $T(\mathbf{r})$, is given by the gas dynamic model for a cold magnetopause by *Kallio et al.* [1997]. Then $g(\mathbf{r}, \mathbf{d}, E) = v/m f_{\text{ENA}}(\mathbf{v}, \mathbf{r})$.

- [12] We only consider the generation of ENAs of energy larger than 50 eV, since at lower energies the angular scattering of the produced ENA increases, invalidating the assumption of the produced ENA having the same momentum as the original proton [see, e.g., *Hodges and Breig*, 1991]. Also, at these low energies the proton-neutral elastic-collision cross sections become comparable to the cross sections for charge exchange [*Noël and Prölss*, 1993].
- [13] The proton bulk velocity, **u**(**r**), is given by an empirical model, based on the Phobos plasma measure-

SSH

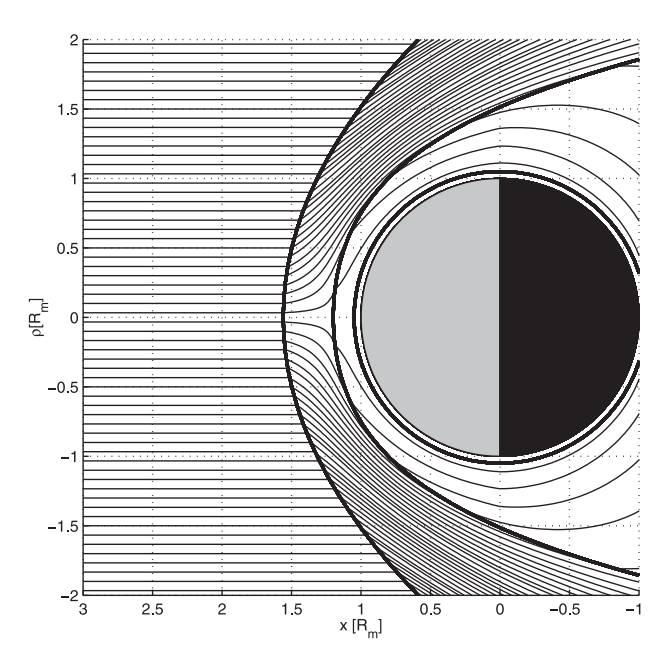


Figure 2. Streamlines for the proton flow around Mars, for the reference values of the parameters in Table 1. The velocity model is cylindrical symmetric around the Mars-Sun line (the x axis). Also shown (thick lines) is the bow shock, the magnetopause (magnetic pile-up boundary) and the obstacle boundary. The units on the axes are Martian radii, R_m .

ments, developed by *Kallio* [1996] and refined by *Kallio* and *Koskinen* [1999]. The velocity is cylindrical symmetric around the Mars-Sun axis. Figure 2 shows an example of the streamlines of the flow, and the boundaries in the model.

- [14] To compute the ENA production rate, $p(\mathbf{r})$, we need to know the proton flux, the density of the neutrals and the charge exchange cross sections.
- [15] The neutral density model includes H, H_2 and O, where thermal and nonthermal oxygen are modeled as two separate species. The atomic and molecular hydrogen models are from *Krasnopolsky and Gladstone* [1996]. The oxygen model is from *Zhang et al.* [1993]. Each specie's density, n_i , is modeled as

$$n_i(r) = N_i e^{-\beta_i \left(\frac{1}{r_o} - \frac{1}{r}\right)} \zeta(\beta_i/r) \quad [\text{cm}^{-3}],$$

where r is the distance to the planet's center, $r_0 = 1.05 R_m$ is the exobase radius, and ζ is Chamberlain's partition function [Chamberlain and Hunten, 1987]. For each neutral specie, we have the constant

$$\beta_i = \frac{GMm_i}{kT_i},$$

where G is the gravitational constant, M is the mass of Mars, m_i is the neutral's mass and T_i is the exobase temperature. From *Kallio et al.* [1997] we have adopted values of the exobase densities N_i and temperatures T_i that corresponds to a case of low solar activity (solar minimum). Due to a lack of data on the exosphere's composition far from Mars, and since the Chamberlain exosphere model does not account

for ionization losses, we have limited the computed ENA emissions to a sphere of radius $20 R_m$ centered at Mars. The error introduced is an under-estimation of the emissions.

[16] The production rate of ENAs from charge exchange with neutral specie i is

$$p_i = n_i \int f_p v \,\sigma_i \,dv \approx n_i \,n \,u \,\sigma_i(u)$$

where σ_i is the energy dependent cross section for charge exchange between protons and neutral specie *i* [Barnett, 1990; Stebbings et al., 1964; Kallio et al., 1997], and for the proton velocity distribution f_p , we have used the approximation $f_p(\mathbf{v}, \mathbf{r}) \approx n\delta(|\mathbf{u} - \mathbf{v}|)$, where $n(\mathbf{r})$ is the proton number density. Summing over all neutral species, we get the ENA production rate, at position \mathbf{r} , as

$$p(\mathbf{r}) = n(\mathbf{r})u(\mathbf{r}) \sum_{i} n_i(r)\sigma_i(u(\mathbf{r})).$$

[17] The proton number density, n, is computed from the velocity field using mass conservation, by integrating the continuity equation

$$\frac{1}{n}\frac{dn}{ds} = -\frac{\nabla \cdot \mathbf{u}}{|\mathbf{u}|} - \sum_{i} \sigma_{i} n_{i} \tag{1}$$

backward along a streamline (arc length *s*), where the second term is the loss of protons due to charge exchange with neutrals along the streamline. An alternative is to solve the continuity equation

$$\frac{\partial n}{\partial t} = -\nabla \cdot (n\mathbf{u}) - nu \sum_{i} \sigma_{i} n_{i} = 0$$

on a grid, starting with the solar wind density at the sunward boundary, and then solve this equation in the antisolar direction.

3. ENA Images

[18] First we present some images and spectra generated by the methods described in the previous section. In Figure 3 we show the view from a distance of 3 R_m looking toward the center of Mars. In what follows, we have used a viewing distance of 3 R_m since it approximately contains the orbit of Mars Express. The different images are for different angles, α , between the view position and the Mars-Sun line. This parameterizes all possible views since our production model is cylindrical symmetric around the Mars-Sun axis. The up direction in the images is perpendicular to the ecliptic plane and the Sun is to the right. In the first image, $\alpha = 80^{\circ}$, ENAs generated behind Mars are faintly visible. The reason is that the proton flow there converges at almost right angle on the Mars-Sun axis (Figure 2). In the second image, $\alpha = 100^{\circ}$, ENAs produced in front of Mars, just downstream of the bow shock, appears. The stronger flux visible at the edge of the field of view is solar wind ENAs, produced upstream of the bow shock. The third image, $\alpha = 120^{\circ}$, is similar, with the emission regions shifted and partially merged. In the fourth image, $\alpha = 140^{\circ}$, the production region down-

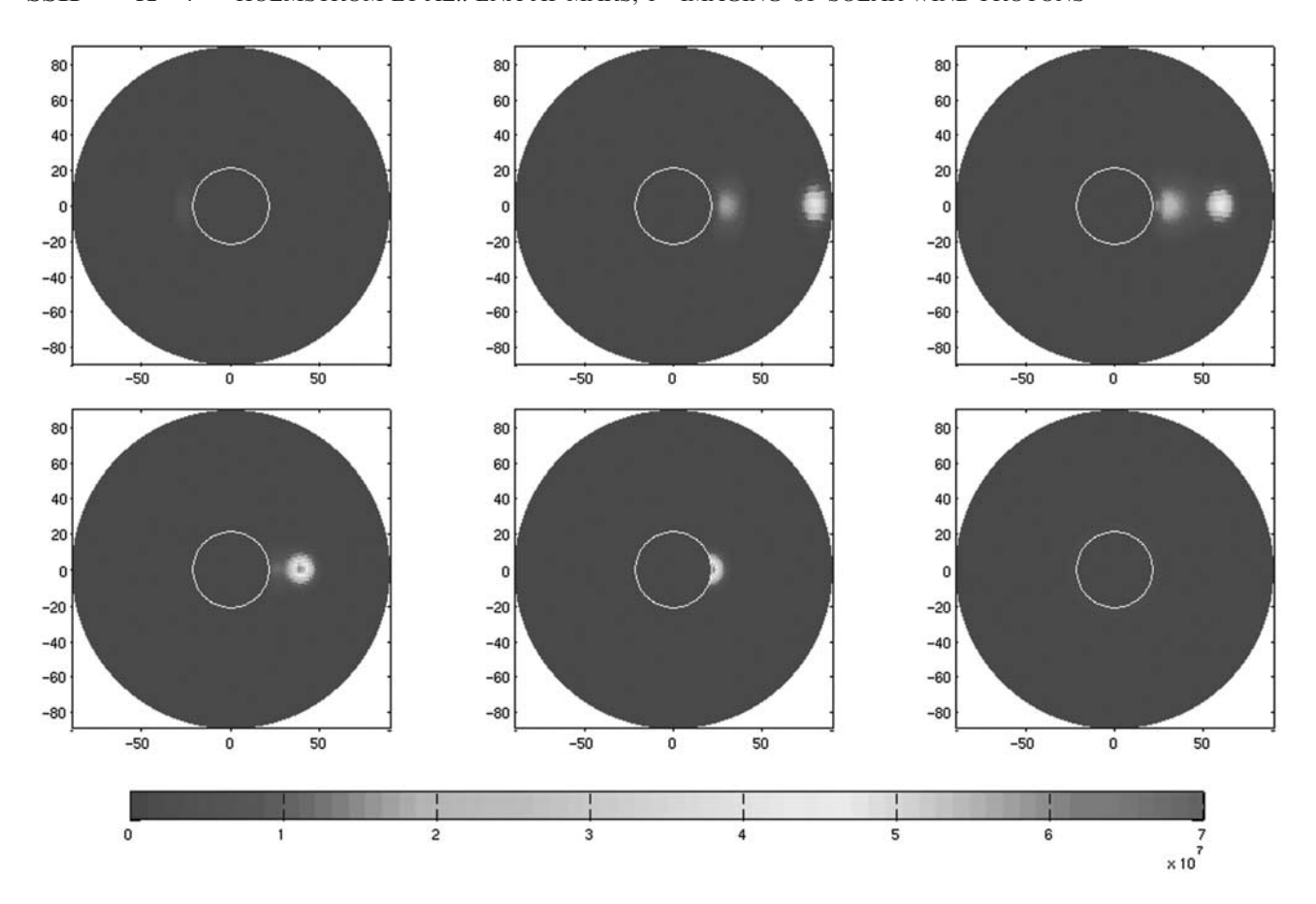


Figure 3. Images of ENA emissions near Mars. The look direction is toward the center of Mars. The view position is at a distance of 3 R_m . The angle of the view position to the Mars-Sun line is, from left to right: top to bottom, 80°, 100°, 120°, 140°, 160°, and 180°. The images have a field of view of 180° and show the intensity (1/(cm² sterad s)) as a function of direction (θ , φ) in a polar format, with the θ coordinate as the polar angle and φ in the radial direction. The axes show the angle to the look direction, φ (deg). The circle is the obstacle boundary, of radius 1.05 R_m . The up direction is perpendicular to the ecliptic plane, along the z axis. See color version of this figure at back of this issue.

stream of the bow shock is mostly invisible behind Mars. The fifth image, $\alpha = 160^{\circ}$, shows the solar wind ENAs setting behind the limb of Mars. In the last image, from the antisolar direction, $\alpha = 180^{\circ}$, we see a halo of ENAs surrounding Mars.

[19] For observational purposes, the total flux of ENAs at a distance from the planet can be of interest. In Figure 4 we show the outflux of ENAs through the surface of a sphere of radius 3 R_m , centered at Mars, as a function of the angle between the view position and the Mars-Sun line. The contributions from upstream and downstream of the bow shock are shown separately. We note that the flux from downstream of the bow shock is maximal at about 115°, while the flux of ENAs produced upstream of the bow shock attains it maximum at approximately 150°. This can be understood from the flow geometry shown in Figure 2. The large flux of protons just downstream of the bow shock, in combination with the denser exosphere close to the planet, is responsible for the first maximum. The solar wind proton flux (upstream of the bow shock) produces the second maximum, at 150° (not at 180° due to shading by Mars). Also shown in Figure 4, for the ENA albedo computations later on, is the ENA precipitation on the

obstacle boundary as a function of solar zenith angle (SZA). The obstacle in the proton flow model, shown in Figure 2, is a sphere of radius 1.05 R_m centered at Mars.

- [20] Examples of ENA spectra are shown in Figure 5. They are directional spectra, along lines of sight, corresponding to the two directions of maximum directional flux in the third image of Figure 3. One toward the production region downstream of the bow shock, and the other toward the Sun. The spectrum in the sun direction is visibly dominated by the solar wind Maxwellian distribution, while the spectrum of the ENAs generated downstream of the bow shock is shifted toward lower energies and decreases more slowly toward lower energies, due to the thermalization of the shocked solar wind.
- [21] We can note that these ENA images and spectra agree well with those computed by *Kallio et al.* [1997] and *Mura et al.* [2002].
- [22] If we follow a proton flow streamline from the solar wind past Mars, protons will be lost due to charge exchange. In our simulations we have accounted for this loss (1), but we have assumed that the velocity distribution is Maxwellian and used the charge-exchange cross sections at the bulk velocity. In reality, the distribution will become non-Max-

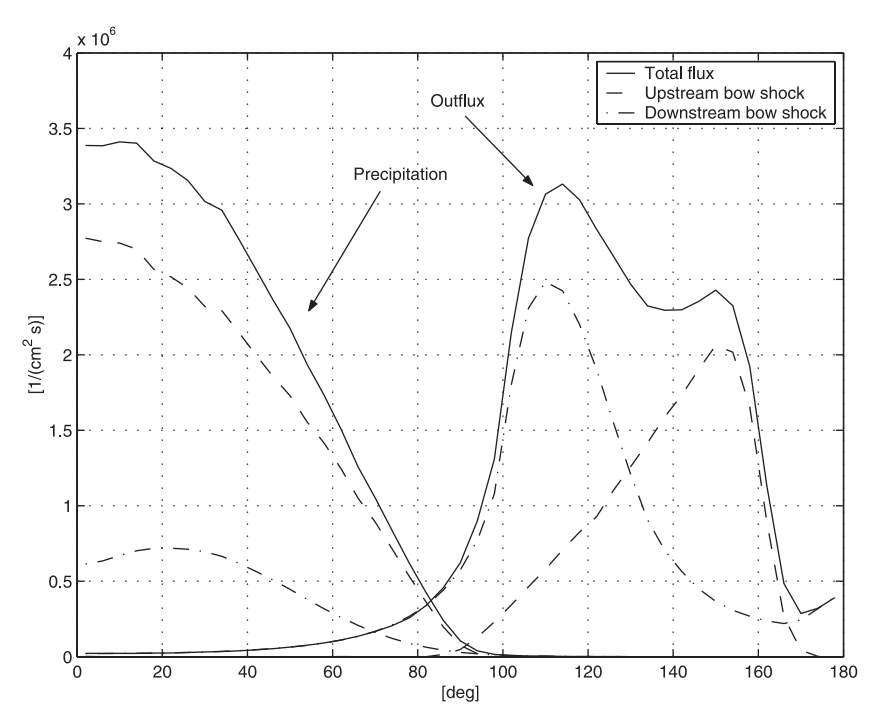


Figure 4. The flux $(1/(cm^2 s))$ of ENAs precipitating on the obstacle boundary as a function of SZA (deg) (shown in the left part of the figure), and the outflux $(1/(cm^2 s))$ of ENAs through the surface of a sphere, of radius 3 R_m centered at Mars, as a function of angle (deg) between the position on the sphere and the Mars-Sun line (shown in the right part of the figure). The solid lines corresponds to the total flux. The dashed lines are the ENAs that are produced upstream of the bow shock. The dashed-dotted lines are the ENAs that are produced downstream of the bow shock.

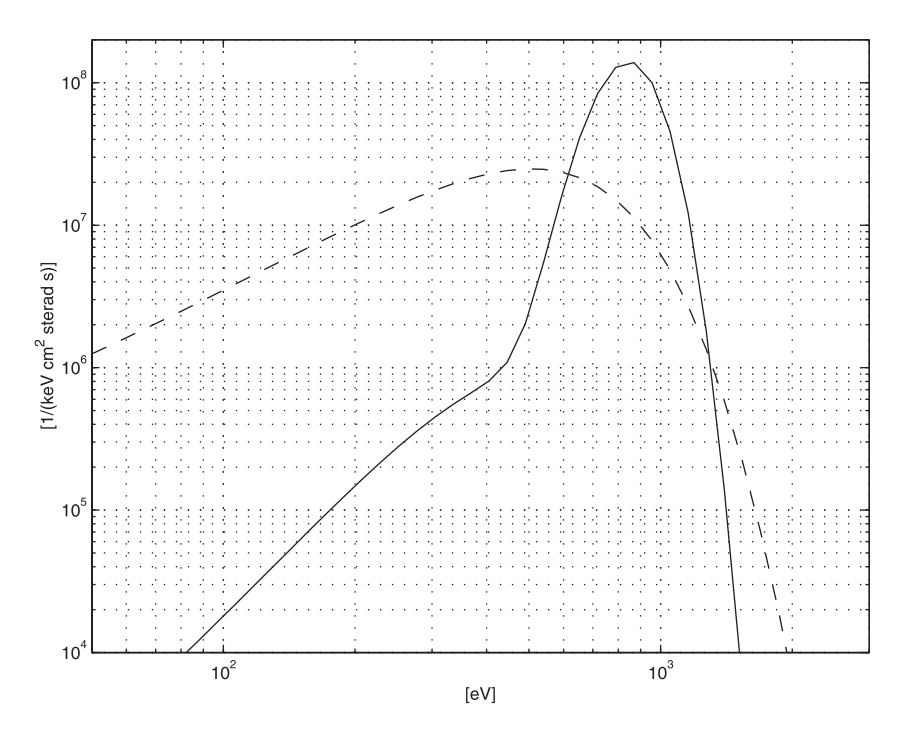


Figure 5. Directional ENA spectra from a view position at an angle to the Mars-Sun line of 120° , at a distance of 3 R_m from the center of Mars. The solid graph is for a view direction toward the Sun. The dashed graph is for a view direction of (1.12, -0.611, 0) toward the area of maximum production downstream of the bow shock. These directions correspond to the two areas of maximum intensity in the third image of Figure 3.

Parameter	Symbol	Reference Value	$ w'(P_i) _{\infty}$	$ w'(P_i) _1$	$p'(P_i)$
Position of the magnetopause		1.2 R _m	7.1	0.67	0.22
H exobase temperature	T_1	192 K	4.6	3.5	3.2
Position of the bow shock	•	1.55 R _m	2.7	1.0	-0.23
Solar wind velocity		400 km/s	2.5	1.6	1.0
Solar wind density		2.5 cm^{-3}	1.0	1.0	1.0
H exobase density	N_1	$9.9 \cdot 10^5 \text{ cm}^{-3}$	0.98	0.92	0.91
Solar wind temperature	•	10 eV	0.92	0.63	-0.16
Magnetopause penetration		1/6	0.45	0.064	0.068
H ₂ exobase temperature	T_2	192 K	0.067	0.083	0.089
O (thermal) exobase temperature	T_{4}	173 K	0.021	0.00078	0.00072
O (hot) exobase temperature	T_3	$4.4 \cdot 10^3 \text{ K}$	0.016	0.011	0.0094
H ₂ exobase density	N_2	$3.8 \cdot 10^6 \text{ cm}^{-3}$	0.014	0.013	0.015
O (hot) exobase density	N_3	$5.5 \cdot 10^3 \text{ cm}^{-3}$	0.0055	0.0042	0.0038
O (thermal) exobase density	N_4	$1.4 \cdot 10^8 \text{ cm}^{-3}$	0.0047	0.00019	0.00014

Table 1. ENA Images' Dependence on the Model's Parameters

wellian, even if it is Maxwellian in the solar wind, since the charge-exchange cross sections are energy dependent, i.e. the charge-exchange efficiency will be different for different parts of the distribution. To estimate the size of this effect we propagated a one-dimensional Maxwellian solar wind velocity distribution along a streamline and observed it downstream of Mars. The velocity distribution was still very close to a Maxwellian, so our assumption that the shape of the distribution is preserved along a streamline is valid.

3.1. Model Parameters

[23] The empirical proton flow model and the neutral model contains several parameters that affect the ENA production. We also have solar wind parameters. The total number of parameters is 14 and they are listed in Table 1, along with reference values that are used in the simulations unless otherwise noted. This set is in no way final. By modifying the underlying models we can introduce new parameters, e.g., ellipsoid shape of bow shock and magnetopause or a parameterized temperature model. In fact, this is one motivation for examining the images' dependence on various parameters: to see where additional parameters could be needed, and find parameters whose values can be kept constant. There are also other parameters in the models that we regard as constants: bow shock shape, magnetopause shape, and the use of the cold temperature model by Kallio and Koskinen [1999]. We also have numerical parameters, e.g., step lengths for the line of sight and streamline integration. In all the presented computations these numerical parameters are chosen such that the numerical error is negligible.

[24] How does the ENA production depend on the parameters? It is important to know since our aim is to extract values of the parameters from observed ENA images. If the images are weakly dependent on a parameter it will be hard, or impossible, to accurately determine the value of that parameter. Thus knowledge of the images' parameter dependence will assist us in the inversion process. Also, although our proton flow model is empirical and does not directly include a Martian internal magnetic field, the effects of such a field can be investigated by changing the existing parameters, e.g., *Liu et al.* [2001] has shown, by simulations, that the presence of an internal field strongly affects the bow shock and magnetopause positions. Therefore we now investigate how an ENA image change when the parameter values change.

[25] Qualitative examples of the images' dependence on two of the parameters, solar wind proton density and bow shock position are shown in Figure 3 along with a reference image corresponding to the third image of Figure 6. The first image is the reference image with the parameter values listed in Table 1. In the second image the bow shock's sub solar height is increased to $0.75\ R_m$ and we observe a slight decrease in intensity and an enlargement of the production region downstream of the bow shock. In the third image the solar wind proton density is increased to $8\ cm^{-3}$, resulting in a corresponding increase in ENA intensity since our model is linearly dependent on the solar wind density. These two cases approximately correspond to the low and high solar wind pressure results presented by *Liu et al.* [2001].

[26] How do we quantify the dependency on the parameters? Given a view point, and view direction, an image, $w(\theta, \varphi, \mathbf{P})$, depends on the vector, \mathbf{P} , of 14 parameters. We examine the difference between a reference image, $w(\theta, \varphi, \mathbf{P}_0)$ and an image where we have perturbed the parameters to $\mathbf{P} = \mathbf{P}_0 + \Delta \mathbf{P}$. To examine the effect of changing each one of the parameters, we choose $\Delta \mathbf{P} = \Delta \mathbf{P}_i$ to be a change of parameter i by an amount ΔP_i . We measure this change, $\Delta w(\theta, \varphi) = w(\theta, \varphi, \mathbf{P}_0) - w(\theta, \varphi, P_0 + \Delta \mathbf{P})$, in L^{∞} (maximum difference) and L^1 (average difference) norms

$$\parallel \Delta w \parallel_{\infty} = \max_{\theta, \varphi} \mid \Delta w(\theta, \varphi) \mid$$
 and
$$\parallel \Delta w \parallel_{1} = \int \mid \Delta w(\theta, \varphi) \mid dA,$$

where $dA = \sin \varphi \, d\varphi \, d\theta$. To account for the different sizes of the parameters we look at the normalized quantity

$$\mid w'(P_i) \mid \equiv \frac{\frac{\parallel \Delta w \parallel}{\parallel w \parallel}}{\mid \frac{\Delta P_i}{P_i} \mid}.$$

Then, for a change, ΔP_i , of parameter *i*, the relative change in the image is approximately $|w'(P_i)| \cdot |\Delta P_i/P_i|$.

[27] Examining this relative change from a certain vantage point will give a quantitative indication of the importance of the different parameters. Table 1 shows results from a view point at a distance of 3 R_m from the center of Mars, at an angle of 120° to the Mars-Sun line, corresponding to the third image of Figure 3. We have used $|\Delta P_i/P_i| = 0.01$.



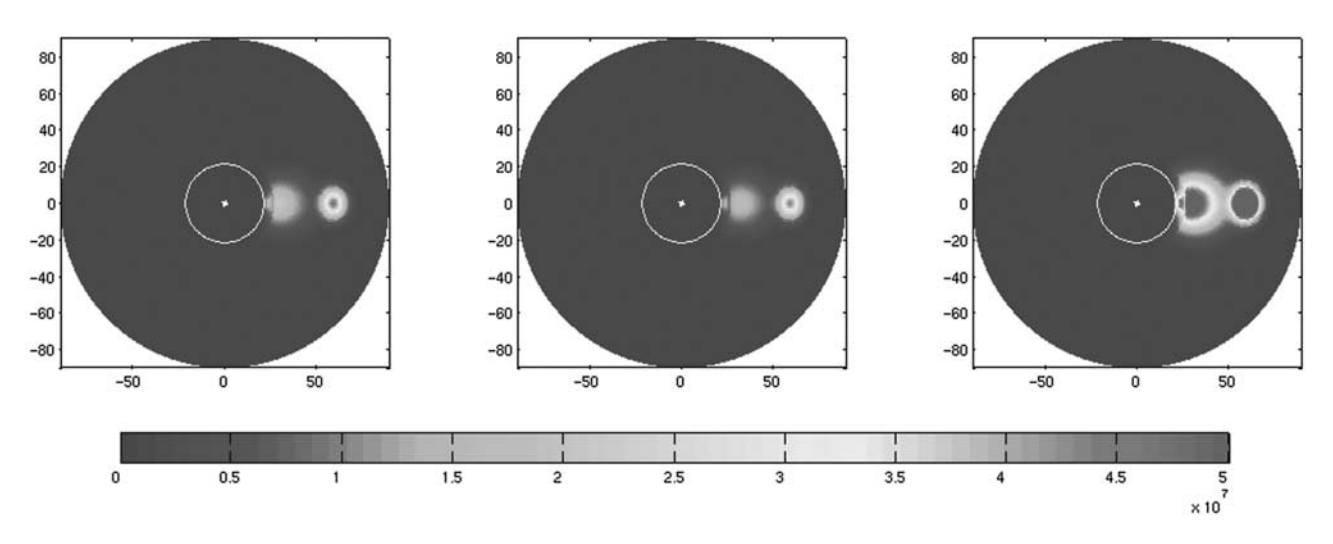


Figure 6. Examples of ENA images' parameter dependence. To the left a reference image that corresponds to the 120° image in Figure 3. The middle image shows the effect of moving the bow shock outward by $0.2 R_m$. The image to the right shows the effect of increasing the solar wind proton density from 2.5 to 8 cm^{-3} . The maximum intensity in the third image is $1.5 \cdot 10^8$ (1/(cm² sterad s)). See color version of this figure at back of this issue.

[28] The parameters in Table 1 are sorted by the maximum directional flux change. First of all we note that changing the magnetopause position produces the largest change in directional flux, although the effect of the magnetopause position on the total flux is quite small. We can explain this by the fact that the volume inside the magnetopause is small, but the production is quite large. The most important parameter in both norms is the atomic hydrogen's exobase temperature. This is natural since hydrogen is the dominating neutral specie at distances from Mars where the proton flux is large. Other important parameters are the bow shock position, the solar wind parameters (proton flux and temperature) and the atomic hydrogen exobase density. We can note that the effect of changing the parameters for molecular hydrogen and oxygen produces ENA image changes that are more than a factor of 10 smaller than for atomic hydrogen.

[29] To investigate the different parameters' effect on the total ENA production, we examine the change in production inside a 3 R_m sphere,

$$p'(P_i) = \frac{\Delta p/p}{\Delta P_i/P_i},$$

and show the result in Table 1. Here p is the total production at the reference state and Δp is the change in production when parameter P_i changes by ΔP_i . Again, atomic hydrogen is most important and the rest of the neutrals relatively unimportant.

3.2. ENA Albedo

[30] Some of the ENAs produced by charge exchange will precipitate on Mars. After interaction (elastic and inelastic collisions) with Mars' atmosphere a fraction of the precipitated ENAs will be emitted again (backscattered), with a different velocity. *Kallio and Barabash* [2000] have investigated the local properties of this process by Monte Carlo simulations and by solving a transport equation. A

global three-dimensional investigation by Monte Carlo simulations is presented by Kallio and Barabash [2001]. In our model we consider the backscattering to take place at the obstacle boundary. The flux of backscattered ENAs in a certain direction at a point on the obstacle boundary is a complicated function of the incoming flux and energy, that in turn depends on the solar zenith angle, and all other parameters in the model. Lacking a good model for this backscatter function, we simplify the problem by using an average ENA albedo value of 0.58 given by Kallio and Barabash [2001], i.e. at each point on the obstacle 58% of the incoming ENAs are backscattered, isotropic. The incoming flux on the obstacle boundary is only a function of SZA, and is shown in Figure 4. To include the ENA albedo in the simulated images, the backscattered flux is added to each line of sight that intersects the obstacle boundary.

[31] In Figure 7 the effect of including the ENA albedo in the simulations is shown. We see that the effect is significant when the angle between the Sun-Mars line and the view position is smaller than 60°, for larger angles ENAs produced in the proton flow dominate. At 60° the maximum flux is from ENAs produced near the magnetopause.

[32] In the empirical model by *Kallio* [1996], as well as in all MHD models of the solar wind flow at Mars, the magnetopause is a tangential discontinuity. That implies no energy transfer across the boundary. However, kinetic (hybrid) simulations indicates that finite gyroradius effects results in energy and particle deposition onto the Martian upper atmosphere [*Brecht*, 1997]. This process will cause an increase of the backscattering ENA flux on the day side and the appearance of an ENA albedo on the night side. While interacting with the atmosphere, precipitating particles go through the cascade of charge-exchange and stripping reactions and almost immediately "forget" their initial charge state. Therefore, we can use the same value of 58% as an estimate of the ENA albedo caused by precipitating protons. The precipitating proton flux given by

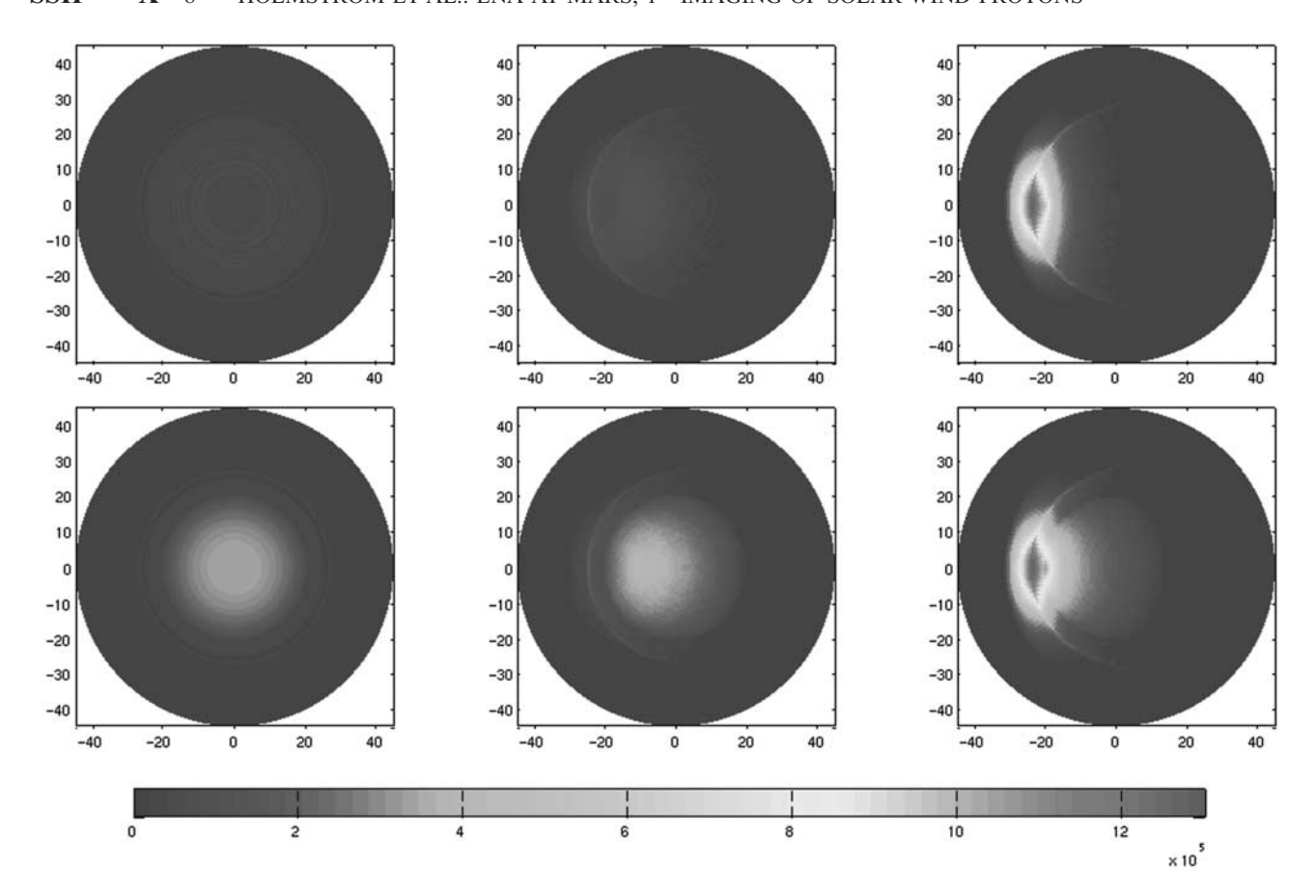


Figure 7. The effect of a 58% ENA albedo. The top row is images without ENA albedo, while the bottom row includes the effect. From left to right, the angle between the Sun-Mars line and the view position is 0° , 30° , and 60° . The images have a field of view of 90° , at a distance of $3 R_m$ from the center of Mars, with the Sun to the left. All other view parameters are identical to those in Figure 3. The unit of the intensity is $(1/(\text{cm}^2 \text{ sterad s}))$. See color version of this figure at back of this issue.

Brecht [1997] is 10^4-10^5 cm⁻² s⁻¹. This can be converted to differential flux by multiplying with $0.58/(2\pi)\approx 0.1$. This flux, 10^3-10^4 cm⁻² sterad⁻¹ s⁻¹, is negligible in comparison with the ENA albedo flux produced by precipitating hydrogen atoms. However, the proton precipitation is highly anisotropic and can result in hot spots on an otherwise smooth ENA albedo distribution.

4. Discussion

[33] We have described an analytical model for simulating ENA images near Mars and shown examples of such images from several view points along with examples of energy spectra. The results are consistent with those computed by *Kallio et al.* [1997] and *Mura et al.* [2002]. An investigation of the total ENA outflux through a sphere of radius 3 R_m show two local maxima, at view points at angles of 115° and 150° to the Mars-Sun line. The first maximum corresponds to ENAs produced downstream of the bow shock, while the second maximum corresponds to ENAs produced upstream of the bow shock in the solar wind. The effect of changing the 14 parameters that our ENA production model depends on was studied. It was found that the shape of the atomic hydrogen density profile is most important, in the sense that a changing the H exobase

density or temperature produces the largest change in the examined ENA image. Other important parameters are the bow shock position and the solar wind parameters (proton flux and temperature). Changes in the density of molecular hydrogen and oxygen had small effects on the ENA images. Note that in practice, the solar wind flux and temperature might not be unknown parameters if measured values are available. We also showed that the effects of the magnetic anomalies on the solar wind-Mars interaction can be approximated by varying the parameters. The effect of ENA backscattering (or albedo) was also studied. We find the albedo clearly visible in the simulated images when the angle between the view position and the Mars-Sun line is 60° or less.

[34] Recent measurements by the Mars Global Surveyor suggest that the solar wind-Mars interaction is more complicated than previously thought, due to localized magnetic anomalies [Acuña et al., 1998]. This has prompted several recent analyses of the interaction [Cloutier et al., 1999; Ness et al., 2000; Vignes et al., 2000]. The anomalies are anticipated to cause some north-south asymmetries, since the crustal magnetic field is mainly distributed in the southern hemisphere [Acuña et al., 1999]. Thus the size of the interaction region can be different in the north and south hemispheres. Also, temporal changes are expected to

take place because the interaction above an anomaly depends on how the IMF is oriented with respect to the crustal magnetic field. Three-dimensional MHD simulations [Liu et al., 2001] have shown that the presence of a planetary magnetic field notably affects the distance of the bow shock and the magnetopause, and the ionospheric scale height. One-dimensional [Kim et al., 1998] and three-dimensional [Hodges, 2000] oxygen corona models shows that the density of the hot oxygen corona strongly depends on the ionospheric losses to the solar wind, and consequently depend on the details of the solar wind-Mars interaction. To a certain extent, the effects mentioned above can be simulated in our model by changing the parameters, but the inclusion of nonaxial symmetry and temporal variations is a topic of future research.

[35] The results presented will guide us in the future work of extracting parameters from ENA images of nonmagnetized planets. A similar model should provide even more accurate images for Venus where kinetic effects are less profound and the crustal magnetization is absent.

[36] **Acknowledgments.** This research was supported by a grant from the Swedish National Space Board.

[37] Janet G. Luhmann thanks K. C. Hsieh and Thomas Cravens for their assistance in evaluating this paper.

References

- Acuña, M. H., et al., Magnetic field and plasma observations at Mars: Initial results of the Mars Global Surveyor Mission, *Science*, *279*, 1676–1680, 1998
- Acuña, M. H., et al., Global distribution of crustal magnetization discovered by the Mars Global Surveyor MAG/ER experiment, *Science*, 284, 790–793, 1999.
- Barabash, S., R. Lundin, T. Zarnowiecki, and S. Grzedzielski, Diagnostic of energetic neutral particles at Mars by the ASPERA-C instrument for the Mars-96 mission, Adv. Space Res., 16, 81–86, 1995.
- Barabash, S., J. Gimholt, and R. Lundin, The analyzer of space plasmas and energetic neutral atoms (ASPERA-3) for the Mars express mission, in *Proceedings of the Workshop on Energetic Neutral Atom Imaging of the Martian Environment, Kiruna, Sweden, September 2–3, 1998, IRF Sci. Rep. 248*, pp. 36–44, Inst. för Rymdfysik, Kiruna, Sweden, 1998.
- Barabash, S., M. Holmström, A. Lukyanov, and E. Kallio, Energetic neutral atoms at Mars, 4, Imaging of planetary oxygen, J. Geophys. Res., 10.1029/2001JA000326, in press, 2002.
- Barnett, C. F., Collisions of H, H₂, He and Li atoms and ions with atoms and molecules, in *Atomic Data for Fusion Ser.*, vol. 1, *Rep. ORNL-6086*, edited by H. T. Hunter et al., Oak Ridge Nat. Lab., Oak Ridge, Tenn., 1990
- Brecht, S. H., Solar wind proton deposition into the Martian atmosphere, J. Geophys. Res., 102, 11,287–11,294, 1997.
- Chamberlain, J. W., and D. M. Hunten, *Theory of Planetary Atmospheres*, 335 pp., Academic, San Diego, Calif., 1987.
- Cloutier, P. A., et al., Venus-like interaction of the solar wind with Mars, Geophys. Res. Lett., 26, 2685–2688, 1999.

- Hodges, R. R., Jr., Distributions of hot oxygen for Venus and Mars, J. Geophys. Res., 105, 6971–6981, 2000.
- Hodges, R. R., Jr., and E. L. Breig, Ionosphere-exosphere coupling through charge exchange and momentum transfer in hydrogen-proton collisions, *J. Geophys. Res.*, *96*, 7697–7708, 1991.
- Kallio, E., An empirical model of the solar wind flow around Mars, J. Geophys. Res., 101, 11,133–11,147, 1996.
- Kallio, E., and S. Barabash, On the elastic and inelastic collisions between precipitating energetic hydrogen atoms and Martian atmospheric neutrals, *J. Geophys. Res.*, 105, 24,973–24,996, 2000.
- Kallio, E., and S. Barabash, Atmospheric effects of precipitating energetic hydrogen atoms on the Martian atmosphere, *J. Geophys. Res.*, 106, 165–177, 2001.
- Kallio, E., and H. Koskinen, A test particle simulation of the motion of oxygen ions and solar wind protons near Mars, J. Geophys. Res., 104, 557–579, 1999.
- Kallio, E., J. G. Luhmann, and S. Barabash, Charge exchange near Mars: The solar wind absorption and energetic neutral atom production, *J. Geophys. Res.*, 102, 22,183–22,197, 1997.
- Kim, J., A. F. Nagy, J. L. Fox, and T. E. Cravens, Solar cycle variability of hot oxygen atoms at Mars, *J. Geophys. Res.*, 103, 29,339–29,342, 1998. Krasnopolsky, V. A., and G. R. Gladstone, Helium on Mars: EUVE and PHOBOS data and implications for Mars' evolution, *J. Geophys. Res.*, 101, 15,765–15,772, 1996.
- Lichtenegger, H., H. Lammer, and W. Stumptner, Energetic neutral atoms at Mars, 3, Flux and energy distribution of planetary energetic H atoms, *J. Geophys. Res.*, 10.1029/2001JA000322, in press, 2002.
- Liu, Y., A. F. Nagy, T. I. Gombosi, D. L. DeZeeuw, and K. G. Powell, The solar wind interaction with Mars: Results of three-dimensional threespecies MHD studies, Adv. Space Res., 27, 1837–1846, 2001.
- Mura, A., A. Milillo, S. Orsini, E. Kallio, and S. Barabash, Energetic neutral atoms at Mars, 2, Energetic neutral atom production near Phobos, *J. Geophys. Res.*, 10.1029/2001JA000328, in press, 2002.
- Ness, N. F., M. H. Acuña, J. E. P. Connerney, A. J. Kliore, T. K. Breus, A. M. Krymskii, P. Cloutier, and S. J. Bauer, Effects of Magnetic anomalies discovered at Mars on the structure of the Martian ionosphere and solar wind interaction as follows from radio occultation experiments, *J. Geophys. Res.*, 105, 15,991–16,004, 2000.
- Noël, S., and G. W. Prölss, Heating and radiating production by neutralized ring current particles, *J. Geophys. Res.*, *98*, 17,317–17,325, 1993.
- Roelof, E. C., Energetic neutral atom image of a storm-time ring current, *Geophys. Res. Lett.*, *14*, 652–655, 1987.Stebbings, R. F., A. C. H. Smith, and H. Erhardt, Charge transfer between
- Stebbings, R. F., A. C. H. Smith, and H. Erhardt, Charge transfer between oxygen atoms and O⁺ and H⁺ ions, *J. Geophys. Res.*, 69, 2349–2355, 1964
- Vignes, D., C. Mazelle, H. Rme, M. H. Acuña, J. E. P. Connerney, R. P. Lin, D. L. Mitchell, P. Cloutier, D. H. Crider, and N. F. Ness, The solar wind interaction with Mars: Locations and shapes of the Bow Shock and the Magnetic Pile-up Boundary from the observations of the MAG/ER experiment onboard Mars Global Surveyor, *Geophys. Res. Lett.*, 27, 49–52, 2000.
- Zhang, M. H. G., J. G. Luhmann, S. W. Bougher, and A. F. Nagy, The ancient oxygen exosphere of Mars: Implications for atmosphere evolution, *J. Geophys. Res.*, *98*, 10,915–10,923, 1993.

M. Holmström and S. Barabash, Swedish Institute of Space Physics, P.O. Box 812, SE-98128 Kiruna, Sweden. (matsh@irf.se; stas@irf.se)

E. Kallio, Finnish Meteorological Institute, Geophysical Research, P.O. Box 503, FIN-00101 Helsinki, Finland. (Esa.Kallio@fmi.fi)

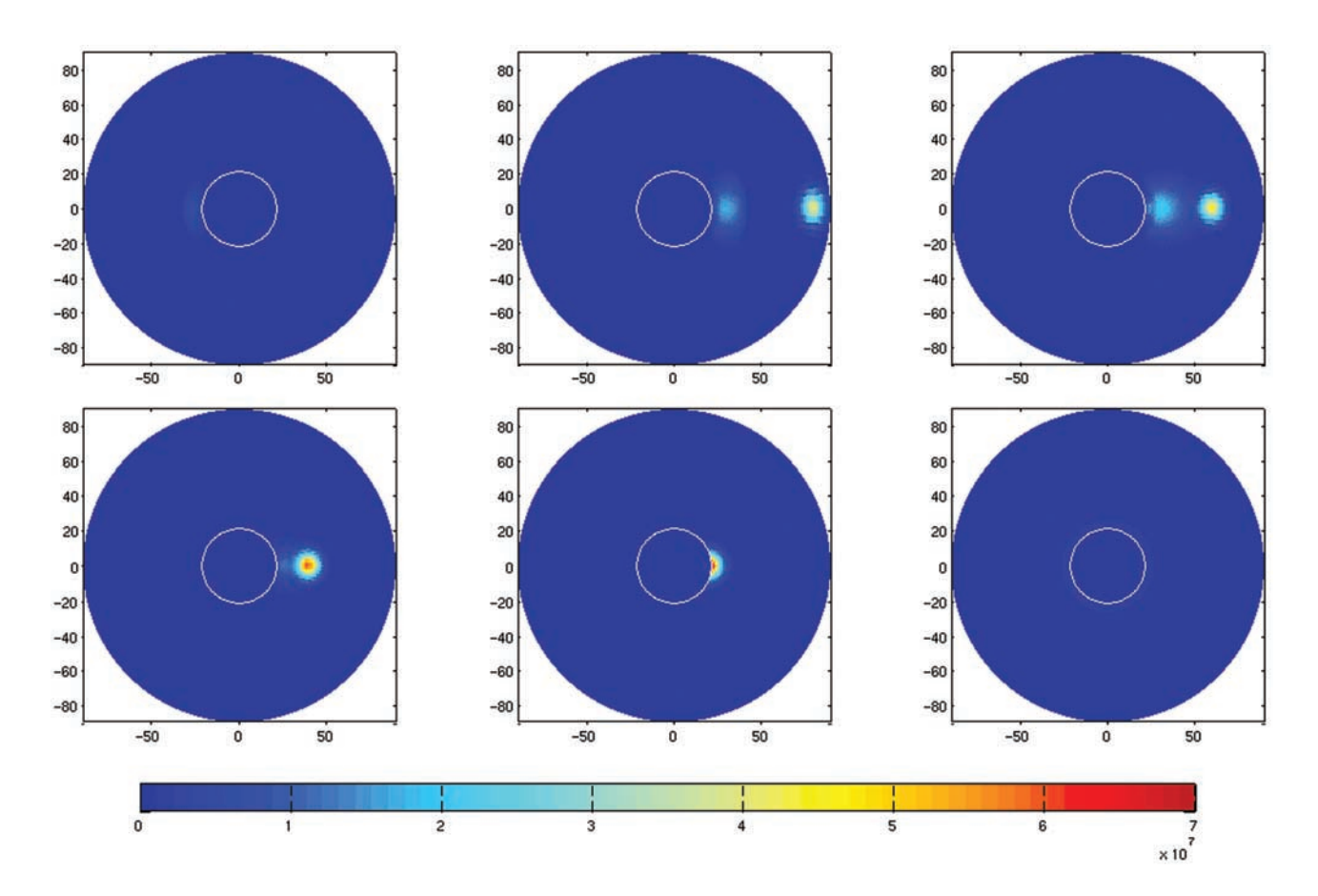


Figure 3. Images of ENA emissions near Mars. The look direction is toward the center of Mars. The view position is at a distance of 3 R_m . The angle of the view position to the Mars-Sun line is, from left to right: top to bottom, 80°, 100°, 120°, 140°, 160°, and 180°. The images have a field of view of 180° and show the intensity (1/(cm² sterad s)) as a function of direction (θ , φ) in a polar format, with the θ coordinate as the polar angle and φ in the radial direction. The axes show the angle to the look direction, φ (deg). The circle is the obstacle boundary, of radius 1.05 R_m . The up direction is perpendicular to the ecliptic plane, along the z axis.

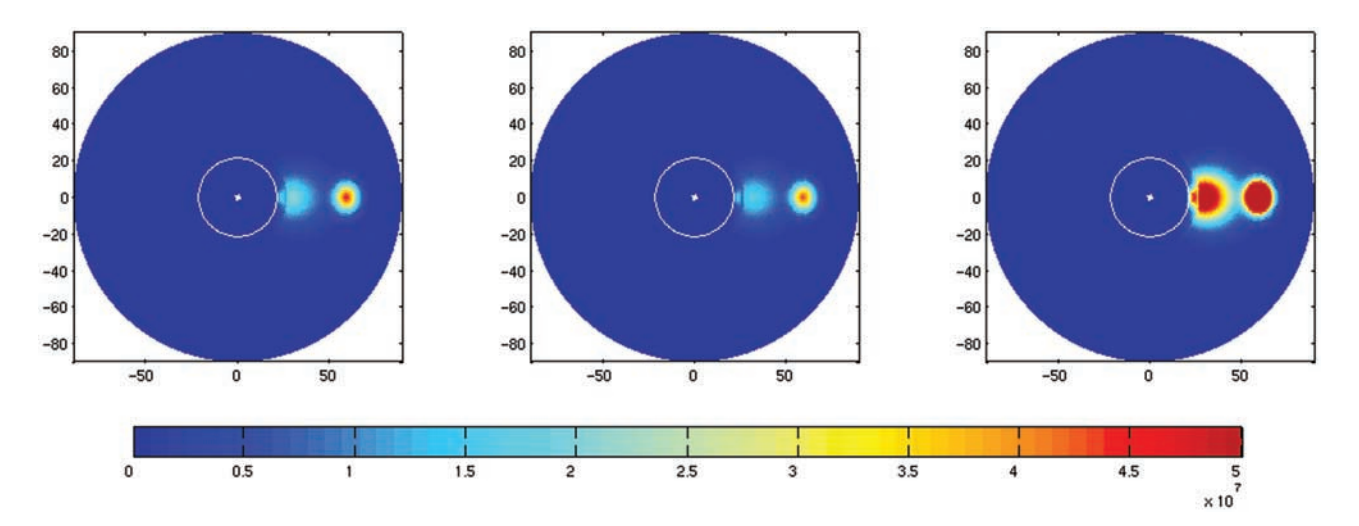


Figure 6. Examples of ENA images' parameter dependence. To the left a reference image that corresponds to the 120° image in Figure 3. The middle image shows the effect of moving the bow shock outward by $0.2 R_m$. The image to the right shows the effect of increasing the solar wind proton density from 2.5 to 8 cm^{-3} . The maximum intensity in the third image is $1.5 \cdot 10^8 \, (1/(\text{cm}^2 \text{ sterad s}))$.

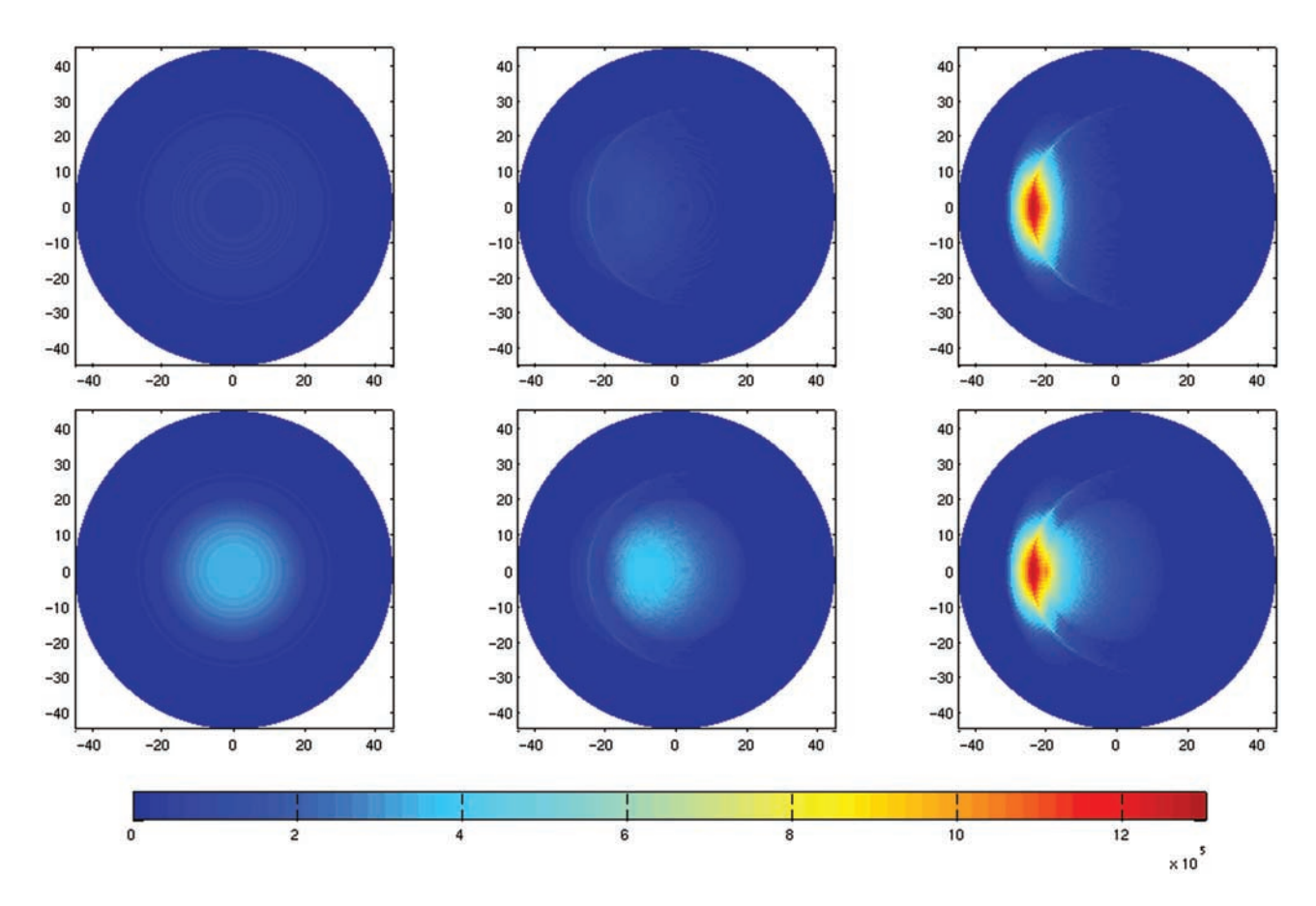


Figure 7. The effect of a 58% ENA albedo. The top row is images without ENA albedo, while the bottom row includes the effect. From left to right, the angle between the Sun-Mars line and the view position is 0° , 30° , and 60° . The images have a field of view of 90° , at a distance of $3 R_m$ from the center of Mars, with the Sun to the left. All other view parameters are identical to those in Figure 3. The unit of the intensity is $(1/(cm^2 \text{ sterad s}))$.